Electronic properties of carbon nanotubes by transmission electron energy-loss spectroscopy

B. W. Reed and M. Sarikaya
Materials Science and Engineering, University of Washington, Seattle, Washington 98195
(Received 3 April 2001; published 17 October 2001)

We present electron energy-loss spectroscopy measurements on isolated single-walled carbon nanotubes and their bundles performed in a scanning transmission-electron microscope. Spectra are obtained over a range of impact parameters, from the centers of the samples to several nanometers outside the material. Curve-fitting techniques reveal five peaks in the range ~2–30 eV. These include surface and bulk plasmons and direct π to π^* interband transitions. The energies, heights, and widths of these peaks are tracked throughout the data sets in order to determine their dependence on bundle diameter and impact parameter. The heights of the externally excited surface mode peaks are compared to a model that varies exponentially with impact parameter and by a power law with bundle diameter. The power-law exponent varies from ~0.4 for the π to π^* mode to ~1.3 for the $\pi+\sigma$ bulk plasmon, with the surface plasmons close to 1. The peak height data suggest a sensitivity to density inhomogeneities in one of the bundles and possibly to random variations in the chiral vectors among the single tubes and small bundles. These patterns are further elucidated in the peak energy and width data.

DOI: 10.1103/PhysRevB.64.195404 PACS number(s): 73.61.Wp, 73.20.Mf

I. INTRODUCTION

Carbon nanotubes have been the subject of an enormous number of studies concerning optimal fabrication, physical structure, and electronic and other physical properties. Not only do nanotubes exhibit remarkable traits that are strongly suggestive for future nanotechnological applications,[1–3] but they are also interesting physical systems in their own right. The theory of the relationship between structural and electronic properties of nanotubes predicts that a tube may be metallic or semiconducting depending on the precise way the carbon hexagons match up around its circumference.[4,5] The effects of interactions within multiwalled nanotubes and parallel bundles of single-walled tubes have also been theoretically investigated.[6,7] Some experimental tests of these theories have been performed, notably in the scanning tunneling microscope (STM) (Refs. 8–10) and the (scanning) transmission-electron microscope with electron energy-loss spectroscopy [(S)TEM/EELS],[11–23] but more work needs to be done. There still exist theoretical predictions that have not been fully tested, as well as experimental results that have not been completely explained by theory. The theory of nanotube EELS in particular needs further development, as there are many inconsistent predictions and a lack of consensus as to what effects should and should not be included in the analysis. This is partially due to a relative lack of experimental results, which could constrain the theory, although this has improved in the last few years.

The STM results have been striking, but carry some limitations. The nanotube must lie on a conducting substrate, which will affect its properties. Quantitative data analysis requires a detailed understanding of tip/nanotube coupling, still an active area of research. Spectroscopy at energies of more than a few electron volts from the Fermi level is quite difficult, and only the outermost atomic layer is directly measurable. TEM/EELS differs from this technique in several ways. The substrate and tip can be eliminated, thus removing all solid material that can mechanically or electronically couple to the section of nanotube under study. The interaction between a material and a passing electron is relatively easy to model, yet is sensitive to interesting effects such as quantum confinement.[24–26] The EELS energy range complements that of STM, starting at a few electron volts and extending to the keV range. This gives us access to the variety of plasmon excitations that occur in nanotubes, as well as the inner-shell edges and direct transitions among the bonding and antibonding bands. TEM also benefits from phase-contrast imaging and nanodiffraction, which are very powerful for analyzing atomic structure and are not limited to the first few atomic layers. Near-future STEM/EELS systems with enhanced spatial and energy resolution[27,28] should extend the measurable energy range and resolution down to small fractions of an electron volt [allowing detailed maps of the substructure of the interband transitions, as is already possible with bulk EELS (Ref. 22)] while providing unprecedented high-resolution images. This will enable determinations of structure-property correlations in a manner not previously possible.

In anticipation of the upcoming improvements in TEM technology, we have undertaken a program to develop techniques for EELS of isolated nanometer-scale structures at very low energies (as low as 2 eV with current systems). The intent is to develop a systematic database of structure/property correlations in order to test theoretical predictions and characterize the results of various fabrication techniques. The current work represents a part of this effort. We report STEM/EELS measurements of single-walled carbon nanotubes, both singly and in bundles ranging from a few tubes to over 100 tubes (diameters from 2.5 to 14 nm, with a single-walled tube being ~1.2 nm across). Multiple measurements are made of each sample, at a variety of impact parameters. Most of the spectra were taken in the aloof mode, i.e., with the probe not intersecting the solid material, and thus characterize the surface charge-density excitations. This technique has a number of advantages, perhaps most important being the dramatic reduction in radiation damage to the sample. Penetrating spectra are also included, which show the bulk excitations. We performed detailed statistical analy-

ses of our data sets, carefully removing the background signal (the tails of the zero-loss peak) and expressing the resulting loss spectra as combinations of individual excitations. We identify five such excitations in the 2–30-eV range, and track their energies, widths, and amplitudes as a function of sample diameter and impact parameter. The range of sample diameters enables one to track the effects of surface curvature, intertube interactions, and tube-to-tube variations that will tend to average out as more tubes are included in the sample. We compare the amplitudes of the various excitations with the results of an elementary quasiclassical theory, and find that the dependence on impact parameter is well modeled by the theory while the dependence on material size is not. This suggests that at these size scales some aspects of the electronic behavior of the material may be well modeled with a simple classical dielectric function, while other aspects may require explicit consideration of the quantum nature of the material. We present evidence that our measurements are sensitive to density inhomogeneities and the chiral vectors of individual tubes.

II. ELECTRON ENERGY-LOSS SPECTROSCOPY OF CARBON NANOTUBES

The electron energy-loss spectra of carbon nanotubes have been experimentally investigated in a number of different ways.[11–23] Instrumentation has included bulk spectroscopy systems, TEM, and STEM. Some investigations carefully control for local geometry, while others generate an average behavior of a relatively large region of material. Both the low-loss (plasmon) spectra and the carbon *K*-shell near-edge fine structure have been studied. The samples analyzed include multiwall nanotubes (MWNT's), single-wall nanotubes (SWNT's), and SWNT bundles, as well as similar systems such as multishelled nanospheres and boron-nitride nanostructures. Some of the results have been contradictory, as have some of the interpretations of the results, partially because there is a lack of consensus as to the appropriate theoretical approach. To establish context for the present work, we shall briefly summarize some of the work published to date.

Kuzuo, Terauchi, and Tanaka[11] performed some of the earliest measurements on MWNT's (following up with SWNT bundles[12]), reporting a $\pi+\sigma$ bulk plasmon at 22–24.5 eV (significantly lower than the values for graphite or amorphous carbon), with a weak shoulder at 13 eV and a π plasmon at either ~5.2 or ~6.4 eV, in a bimodal distribution. Most of these results (excepting the bimodal distribution) have been reproduced numerous times, although the interpretation of the 13-eV peak has been ambiguous. The carbon *K*-edge spectra show a broadening at smaller diameters, and this too has been reproduced, but not universally.[13–16] Interpretations range from curvature effects to intershell interactions to the presence of amorphous carbon. Similar results[14] show the $\pi+\sigma$ plasmon peak lowering in energy as the diameter of the MWNT is reduced. They interpret this as a curvature effect, altering the delocalization of the π electrons, although similar effects have been interpreted elsewhere as a gradual replacement of bulk-plasmon intensity for surface-plasmon intensity.[17] The surface plasmon was separately identified in 1994.[18]

In 1993, Cullen and coworkers[15] reported on the positional dependence of both the low-loss and carbon *K*-edge EELS, noting an apparent shift in plasmon energy and π^* peak strength between the edge and the center of a MWNT. These effects are investigated systematically in the more recent efforts of Kociak *et al.*,[19] who explain the effects in terms of the anisotropic behavior of the graphene sheets, considering the different local orientation at the edges and centers of the MWNT's. This work identifies two major $\pi+\sigma$ surface plasmons at different energies, with different polarizations. Stéphan *et al.*,[16] by comparing results from MWNT's and isolated SWNT's, contributed evidence that curvature and intershell interactions affect the σ^* much more than the π^* orbitals and call into question some earlier interpretations. MWNT's, SWNT's, and multiwalled carbon nanospheres have been measured at high spatial resolution,[20] showing apparent shifts in plasmon energies that may be explained using straightforward dielectric models. Differences have been noted in the carbon *K*-edge fine structures for bent and straight nanotubes.[21] There have also been bulk EELS measurements at high energy and momentum resolution,[22] showing dispersion relations for the bulk plasmons seen by other groups, plus a series of sharp π to π^* transition peaks in the range ~1–3 eV.

The theory of EELS in nanotubes and other nanometer-scale structures also forms quite an extensive amount of literature.[20,29–38] Particularly fruitful has been the quasiclassical dielectric approach, which has the twin virtues of being easy to understand and apply, yet sufficiently accurate to capture much of the interesting real-world phenomena. The effects of local geometry, material anisotropy, spatial dispersion, and relativistic retardation may all be incorporated into the theory as required. Of these, all but the last will likely be of importance for the kind of measurement we are presenting. The theory assumes that the material properties may be represented by a classical dielectric function, with a clear distinction between surface and bulk charge densities, and that quantum mechanics need only come into play in identifying a frequency ω with an energy $\hbar\omega$. Once these assumptions are made, one must simply compute the field due to the passing charge, determine in a self-consistent way the charge density within the sample, and calculate the work done on the electron as it passes by.

It is not obvious that this formalism should apply without modification to a single-walled carbon nanotube, which is only one atomic layer thick. Also, in order to apply the formalism, one requires a reliable dielectric function, and this is problematic in the case of nanotubes. There have been a number of theoretical calculations of band structures and dielectric functions, including local anisotropy and spatial dispersion in some cases,[4–6,39–41] but they each use different methods and arrive at very different results. Experimental confirmation of these dielectric functions is incomplete. Reliable dielectric functions for nanotube bundles are similarly difficult to obtain. The bundles are locally anisotropic in a complicated way, including highly curved sections of graphene sheets with a variety of orientations in close prox-

imity to one another. It may be that a formalism that works for a large bundle by dealing with anisotropy by producing a ''macroscopic'' average will fail for a small bundle or a single tube. Further, if a sample contains a random mix of nanotubes with different chiral vectors, one might find that the sensitive dependence of the π and π^* bands on chiral vector[4,5] may average out in the larger bundles, while producing idiosyncratic behavior in small bundles or single tubes. As we shall demonstrate, our data sets do suggest such an interpretation. We also find that the dependence of excitation amplitudes on material diameter contradict an elementary quasiclassical model, suggesting that the material properties may have to be treated in an explicitly quantum-mechanical framework.

III. EXPERIMENTAL METHODS

The single-walled carbon nanotube material was produced by pulsed dual-laser vaporization, and purified with nitric acid reflux, followed by washing/centrifugation cycles, and cross-flow filtration.[42,43] The nanotubes were formed into $\sim$1-μm-thick paperlike sheets by vacuum filtration of nanotube suspension through a poly(tetrafluoroethylene) filter, using a process similar to those found in the literature.[42,43] The sheets were heat treated in argon at 1100 °C for one hour. The material was stored under vacuum. The resulting material is almost entirely composed of bundles of single-walled nanotubes (with some isolated single tubes as well), and seems to be of high quality with regard to bonding and crystallinity, although the chiral angles appear to be somewhat random.[23] Metallic inclusions, ''bucky ball'' impurities, and other contaminants were sufficiently rare as to be easily avoided in the selection of regions for analysis, and amorphous surface contamination was minimal.

The sheets were prepared for TEM by shredding with sharp tweezers and enclosing the pieces within folding caged copper grids. Our experience is that this technique is much faster, easier, and less prone to contamination than the more common method of placing drops of suspension on holey carbon grids. The material is free-standing and does not require a substrate, and displays no tendency to charge up during irradiation. Suitable subjects for analysis are easily found at the edge of each piece of nanotube paper. The samples were shredded freshly, less than ten minutes before being placed in the ultrahigh vacuum (UHV) load-lock chamber. Once under vacuum, the samples were baked at 120 °C for roughly one hour, then left overnight at UHV. Typical images are shown in Fig. 1.

The measurements were performed on an instrument at Cornell University (VG HB501 UHV STEM equipped with serial and parallel EELS) with an incident energy of 100 keV. We used an objective aperture of 2.5 mrad and a collector aperture of 1.8 mrad (which is much larger than a typical scattering angle for low-loss EELS). The electron probe was 0.2 nm in diameter. For our measurements, we required a very sharp cutoff of the energy tails of the zero-loss peak, very large dynamic range (to allow simultaneous measurement of the zero-loss peak and the much weaker loss electrons), a linear response at very low counting rates, and consistent performance from measurement to measurement that would not be compromised by analog drift in the detectors. A failure to achieve any of these would have hopelessly obscured the weak signal at very low-energy loss. For this particular instrument, this implied that the EELS should be done in a serial pulse-counting mode. The parallel mode did not offer the required dynamic range, energy resolution, or consistent zero level, and the serial analog mode became nonlinear at low intensities. The pulse-counting spectra were statistically very well behaved, the uncertainties being precisely quantifiable, as we shall discuss in the next section. This, and the very high sensitivity and linearity at low signal levels are what allowed us to extract the energy-loss functions down to $\sim$2 eV with high confidence and analyze them reliably as sums of discrete excitations, even for samples as small as an isolated single-walled tube. The energy resolution [full width at half maximum (FWHM) of the zero-loss peak] was $\sim$0.6 eV. The spacing between measurements was 0.2 eV.

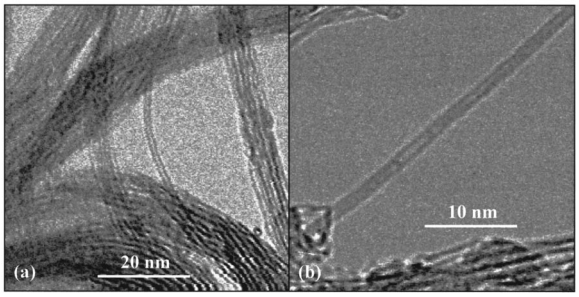

FIG. 1. STEM bright-field images of single-walled carbon nanotubes and nanotube bundles.

Most of the measurements were performed in the aloof mode (with the electron beam not penetrating the material). This has several advantages. Sample damage and contamination (due to pinning of impurities in the vacuum) are greatly reduced. The material is not heated to as high a temperature, which reduces the tendency of the sample to move during a measurement (which can be very significant for the long, thin nanotubes and bundles). Only surface modes are excited, and typically only at relatively small wave vectors, which simplifies both the data interpretation and the theoretical analysis. Previous results have shown that, in many cases, the aloof spectrum is well modeled by the simple quasiclassical approach mentioned in the preceding section, and yet the technique is still sensitive to interesting effects such as quantum confinement, surface effects, and relativistic retardation.[24–26,30–37,44,45] We also took spectra with the beam penetrating the material, in order to obtain information about the bulk excitations. These spectra were typically less repeatable and harder to interpret than were the aloof spectra.

Every spectrum was taken with before-and-after images [STEM annular dark field (ADF)], with the center of the probe placed at a specific pixel in these images for the EELS acquisition. This provides a record of drift, sample damage, and contamination accumulation for each measurement. Most of the time, the position drift was a small fraction of a nanometer for an acquisition lasting roughly two minutes, and in such cases we took the impact parameter to be the average for the before-and-after images. For much larger

amounts of drift, we discarded the spectra, as there was no way to determine an effective average impact parameter. We also discarded spectra if noticeable amounts of contamination appeared in the after image (if it appeared in the before image, the spectra were simply aborted, and a new sample position was chosen). After the sample had spent some 24 h in the UHV chamber, mobile contaminants that could be pinned by the electron beam were almost nonexistent.

The beam current was kept fairly low to avoid damaging the sample. We observed damage thresholds in both beam current and direct irradiation time, and the most common form of damage we noticed was a simple vanishing of material. With the beam current well below threshold, we observed no apparent damage even after many minutes of direct irradiation. These results suggest that the material has to reach a certain temperature before the carbon atoms start to leave the sample; whether this is a result of sublimation, some sort of thermally enhanced knock-on damage, or some other mechanism, is unclear. It is harder to determine whether the atomic structure was being changed over time by the irradiation. However, such damage could, to some extent, be detected by changes in before-and-after phase-contrast images and by watching for shifts in plasmon energies over time as, e.g., graphitelike amorphous carbon has significantly different plasmon energies than do single-walled carbon nanotubes. We saw no such effects even after long exposures (tens of minutes), leading us to think that radiation damage was kept to a minimum. The threshold voltage for knock-on damage in graphite has been reported to be as low as $\sim 50-60$ kV.[46] It is therefore preferable to operate in the aloof mode, so far as sample damage is concerned.

Each nanotube or bundle was selected carefully for uniformity and cleanliness of appearance, isolation, straightness, and being rigidly supported at both ends (which dramatically reduces the motion of the sample). Where practicable, the motorized stage (a prime source of drift) was allowed to sit for some hours or even overnight before the actual EELS measurements were taken. Each measurement series consisted of a set of zero-loss background spectra taken tens of nanometers from any solid material, followed by a scan across the sample with spectra taken roughly once per nanometer starting three or four data points off the right edge of the material, passing through it, and ending three or four data points off the left edge, and a concluding set of zero-loss measurements. Provided there were no tip flashes, spectrometer refocuses, etc., between measurements, all of the zero-loss background spectra were equivalent, to within random error consisting of Poisson statistics and small point-to-point energy drifts (as we discuss below). The beam could be reaimed by many tens of nanometers without producing enough aberration to distort the measurements.

A consistency check was performed by a symmetry requirement: The spectra from the second half of the series should be identical (within error) to those from the first half. In a few cases they were decidedly not. These cases tended to show either unusual levels of contamination pinning or excessive drift (presumably due to heating) when the beam penetrated the material. In extreme cases, the apparently overheated material produced an excessively noisy spectrum, with quasiperiodic peaks superimposed on a more ordinary spectrum. This effect abated some ten minutes after direct irradiation.

In any case, the spectra that were clearly contaminated in some way or another were discarded. An additional consistency check was made in one case by performing two complete series on the same single nanotube. The two series produced substantially the same results, within our uncertainty estimates. These series are plotted together on one of the graphs for the 1.2-nm-diameter nanotube, presented below, where the inter- and intraseries variations may be directly compared. Thus the sources of uncertainty that we calculated appear to account for much of the random error in the data.

IV. DATA ANALYSIS

In order to accurately measure the transitions associated with the π electrons at very low energy (2–6 eV), it was necessary to subtract the zero-loss background from the low-loss spectra. Standard deconvolution methods[47] were found to be inadequate in that they either generated artifacts and noise or failed to completely remove the background in the energy range of interest (as tested by removing the background from a pure-background spectrum). Instead, we resorted to a curve-fit procedure similar to one reported in the past,[36] and which will be discussed in detail in a separate paper in the near future. The procedure consists of fitting a separately measured background spectrum (interpolated with a spline to allow continuous shifting in the energy axis) to the elastic peak in a low-loss spectrum, and subtracting. Meaningful values can be extracted to an energy loss as low as ~ 2 eV in the FEG system we used, although the uncertainties in the 2–2.5-eV energy range tend to be quite large.

The uncertainty in each data point was found to be adequately modeled by a combination of counting statistics (easily quantified since we operated in a pulse-counting mode) and a random energy drift from data point to data point with a standard deviation of ~ 0.07 eV. The dwell time at each data point was 0.5 s and an energy jitter of this magnitude at this time scale is not too surprising. The normalized residuals, defined as the difference in the fit and measured curves divided by the uncertainty function, showed essentially random noise when fitting two background spectra to each other. The quantity χ^2/υ (with χ^2 defined as the sum of the squares of the normalized residuals and υ as the number of data points minus the number of fit parameters) was consistently near unity in such cases, as it should be.[48] The accuracy of counting statistics and the stability of the detector gain were tested with long-time series measurements of the detector dark counts. No significant variation from Poisson statistics with a constant mean was discerned over any time scale relevant to our measurements.

Once the elastic background was removed and the uncertainties were established, the data were normalized by dividing by the integral of the complete spectrum, and then analyzed by curve fitting to a sum-of-Lorentzian peaks (an appropriate functional form for exciting a discrete set of damped quantum harmonic oscillators):

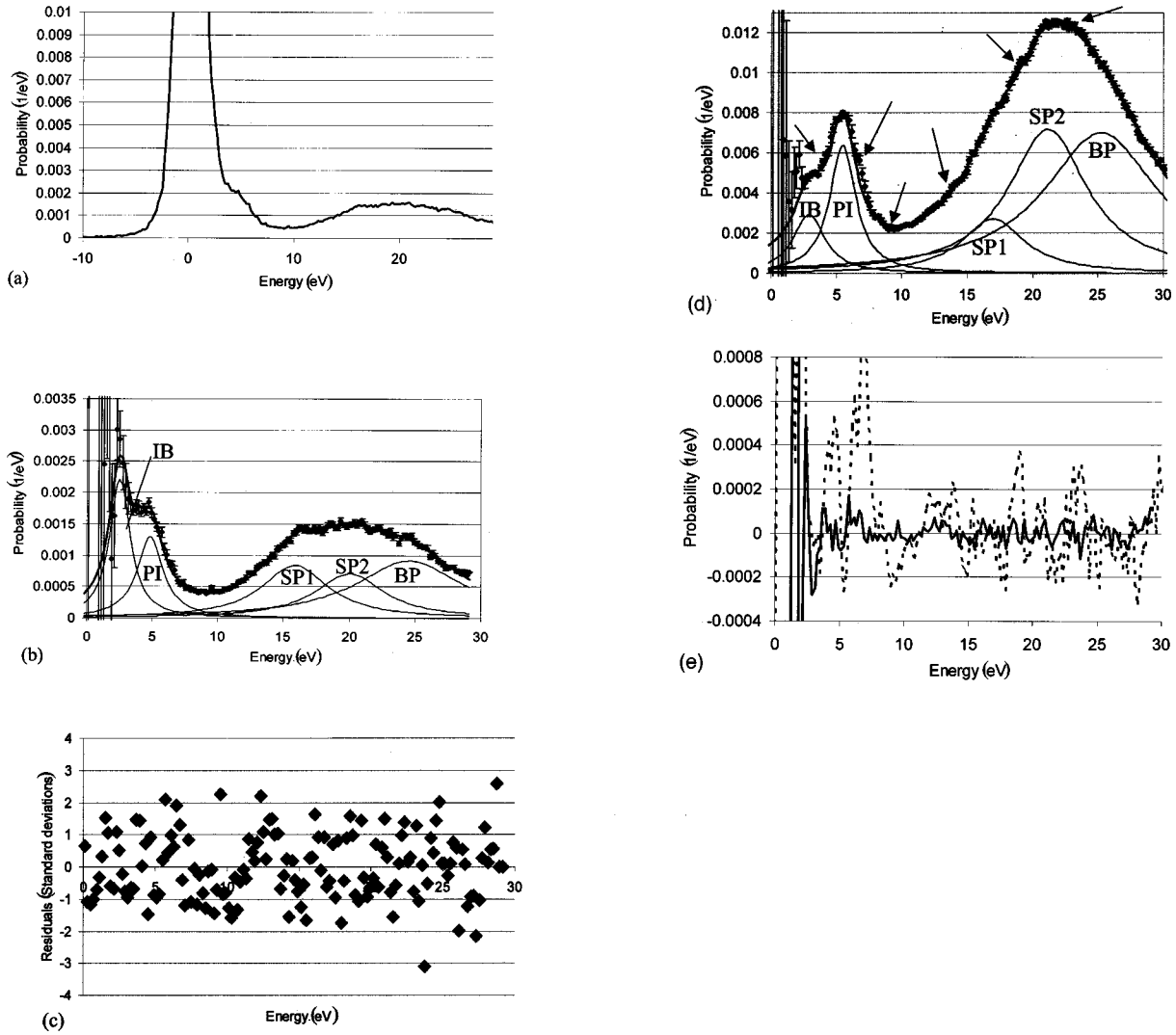

FIG. 2. (a) Typical normalized low-loss spectrum, as measured. (b) After background subtraction, with Lorentzian peaks and sum-of-Lorentzian fit curve superposed. (c) Normalized residuals, showing a near-random scatter and an rms value close to unity. (d) A spectrum generated by penetrating over 10 nm of material (near the middle of a bundle of diameter 14 nm), with the best-fit Lorentzian model not capturing all of the detail. Regions with consistent patterns exceeding roughly two standard deviations in each data point are shown with arrows. (e) Raw residuals from the curve fits in (b) (solid line) and (d) (dashed line). See Table I for peak identification codes in this figure and all the figures that follow.

$$f(E)=\sum_j \frac{A_j W_j/2\pi}{(E-E_j)^2+(W_j/2)^2},$$

where E_j and W_j are the energy and full width at half maximum, and A_j the total area under the curve, for excitation j. Since the spectra are normalized, A_j is equal to the total probability of exciting mode j (under the Lorentzian approximation). Due to a nonlinearity at high counting rates, the resulting A_j values are slightly overestimated. The peak height $B_j=2A_j/\pi W_j$ is a more relevant parameter than A_j for some theoretical comparisons. We found that most spectra could be fit quite well with as few as three and no more than five excitations, with the residuals in many cases being reduced to little more than random noise (as determined by calculating χ^2 using our previously determined uncertainty estimates). Figures 2(a)–2(c) demonstrate this for some typical spectra. Some spectra could not be fit adequately even with five Lorentzians—the fit function $f(E)$ is not entirely appropriate for these cases. Figure 2(d) shows a typical case, in which the electron beam is penetrating ~10 nm of material (near the middle of a large bundle). The plasmon peaks are quite asymmetric and irregular, showing a complex structure. The sum-of-Lorentzian function captures the basic shapes of the peaks but misses the substructure. The arrows in Fig. 2(d) indicate places where the curve fit fails to capture the detailed shape of the spectrum by about two or more standard deviations over several consecutive data points. The substructures at roughly 4, 6, and 13 eV are repeatable from one spectrum to another, appearing in essentially every spectrum measured with a sufficient signal-to-noise ratio. The 13-eV peak may be the same as the weak shoulder observed at this energy by other researchers.[11,12] χ^2/v for the spectrum

in Fig. 2(d) was 2.66; this is a typical value for the deep penetrating spectra, which showed strong signals and quite a lot of substructure in the peaks. For the cleaner curve fits generally penetrating little or no material, χ^2/v was usually in the range 0.9–1.5. This is only very slightly more than would be expected for the ~140 degrees of freedom in each fit, thus the fit is capturing the great majority of the information in the spectrum. The error bars for most data points are dominated by counting statistics. We also include nonnormalized residuals for both of these curve fits in Fig. 2(e).

Deconvolution with the zero-loss peak was not performed, for two reasons: (1) The results would not be reliable, as the detector became highly nonlinear at high count rates, so that the shape of the zero-loss peak was not accurately measured, and (2) it would have little effect, since all of the reliably measured W_j's were much larger than the zero-loss FWHM of ~0.6 eV, and these widths add in quadrature during the convolution. Deconvolution as a means of removing the quasielastic background was found to be less effective and more error-prone than the spline curve-fit technique.

Interpretation of the curve-fit parameters is complicated, and to avoid misunderstanding we must explain some of these complications before proceeding to the actual results. The uncertainties in the curve-fit parameters were calculated via the diagonal elements of the inverse of the second derivative matrix of χ^2, according to the procedure given by Bevington.[48] In many cases the off-diagonal elements were significant, so that the diagonal components were not a complete representation of the uncertainty of the parameters. In other words, the fit parameters mutually interact, especially for peaks that largely overlap with one another, and the uncertainties we report may be regarded as lower limits in such cases.

The choice of the number of Lorentzian peaks to use in the fits was sometimes clear-cut and sometimes rather arbitrary. An isolated symmetric peak requires at least one Lorentzian, an asymmetric peak at least two, and this gives a lower limit to the number of Lorentzians required to model a given spectrum. In some cases this minimal number gave a χ^2/v value close to 1, which was not improved significantly by adding more Lorentzians, and which gave no clear pattern in the normalized residuals. These were the easy cases. More commonly, adding one or two Lorentzians into the mix significantly reduced both χ^2/v and the patterns in the normalized residuals, causing a formerly single peak to be reinterpreted as two or three separated peaks, one or more of which may have a height differing from zero by less than two standard deviations. When faced with a choice of two curve fits, which seemed to account for the data roughly equally well, we tended to choose the one which gave the most continuity when compared with neighboring spectra. For example, if two spectra show that a peak at 14 eV can be resolved into two Lorentzians at 12 and 15 eV, and a spectrum taken in between these two positions shows an asymmetric peak at 14 eV that, according to the statistics, can be modeled almost as well by one Lorentzian as by two, we chose to model it with two. In the future, we would like to use the mathematical techniques associated with spectral imaging to help us make these decisions more objectively. In cases where even five Lorentzians could not model the spectrum adequately, we decided that the sum-of-Lorentzians fit function is no longer appropriate, as the parameters in six or more overlapping peaks can no longer be taken to have any individual validity for data such as ours. This typically happened for the deep penetrating spectra, which can be expected to include many excitations, both surface and bulk, with significant spatial dispersion effects. Still, even in these cases, the curve fit captures most of the variation, as Fig. 2 shows.

This brings us to an additional advantage of aloof over penetrating EELS (besides the reduction in sample damage and heating). The aloof signal does not contain bulk excitations, and is entirely due to surface modes associated with plasmons and interband transitions. Thus there are inherently fewer excitations in the aloof case, allowing much cleaner and more reliable curve fits and simpler theoretical analysis. The effect of spatial dispersion, which can create asymmetries in the peaks, is also reduced when the beam does not penetrate the material. The aloof spectra were generally much better modeled with a sum of Lorentzians than were the penetrating spectra. This means we can analyze the surface modes, cleanly separating them one from another, using the aloof technique. Then, if we want to know more about the bulk modes or the surface modes at high-momentum transfer, we can use this understanding of the surface modes to assist in interpretation of the penetrating EELS. Advanced spectral-imaging data analysis techniques should be helpful with this as well. The combination of aloof and penetrating EELS provides a more complete picture of the material than would either technique by itself.

V. RESULTS

The bulk of the data could be reduced to Lorentzian curve-fit parameters and χ^2/v values (which specify how well the Lorentzians describe the data) as a function of bundle (or tube) diameter and impact parameter. We identify up to five peaks in each spectrum, and classify them according to the scheme in Table I, illustrated by a typical spectrum in Fig. 2(b). Other minor features occasionally appear, as seen in Figs. 2(c) and 2(e), but generally with inadequate signal-to-noise ratio to warrant detailed analysis. The interband (IB) peak is rarely cleanly separated from both the inelastic background and the π plasmon (PI) peak, due to counting statistics and asymmetry in the π plasmon peak. The term ''IB peak'' refers to a component included in the curve fit, which roughly accounts for the intensity in the

TABLE I. Peaks used in the sum-of-Lorentzians curve fit.

Identifier	Typical energy (eV)	Description
IB	2–3	π to π^* interband transition
PI	4.5–5.5	π plasmon
SP1	13–15	$\pi+\sigma$ surface plasmon, low-energy mode
SP2	17–19	$\pi+\sigma$ surface plasmon, high-energy mode
BP	23–27	$\pi+\sigma$ bulk plasmon

1.5–4-eV range that is not accounted for by the background and the PI peak. The fit parameters for this peak must be taken with some skepticism. The extracted value for the energy, for example, is usually higher than it probably should be, and is definitely not independent of the PI energy. However, the χ^2/v values suffer noticeably when this peak is not included in the fit, and the peak amplitude tends to differ from zero by at least three standard deviations. Moreover, the peak does not appear when fitting background spectra to each other, leading us to conclude that this is no mere artifact of the background subtraction technique. In accord with previous theoretical[6,39] and experimental[22] results (such peaks have been observed in bulk EELS), we identify this peak as arising primarily from π to π^* direct interband transitions. The relative visibility of such peaks should be strongest for aloof measurements of subjects with very small diameters,[36] which agrees with our observations.

The PI peak is a combination of the surface and bulk collective modes of the π electrons. The energy difference between the surface and bulk modes is too small to permit a clear separation of the two. The bulk mode should be at a slightly higher energy, which may explain an apparent upward shift in energy for penetrating as opposed to aloof spectra at large bundle diameters (described below). The complete set of all of the π and σ valence electrons will also show collective excitations, which we can separate into two surface plasmons, (SP1) and (SP2), and a bulk plasmon (BP). It is not always possible to separate these three excitations in a clean and unambiguous way. Kociak *et al.*[19] have performed similar measurements on multiwalled nanotubes, identifying plasmons at roughly the same energies that we observed. Their ~14-eV peak is identified as a surface plasmon associated with π-σ^* and σ-π^* excitations normal to the plane of the graphene layers, and their ~18-eV peak is taken to be a σ-σ^* in-plane surface mode. They also report a shift of the bulk mode from 23 to 27 eV between the edge and the center of the material. These effects are due to anisotropy within each graphene plane. We see remarkably similar behavior in the bundles of single-walled tubes, which is interesting since the anisotropy of the bundles and of the multiwalled tubes should be of rather different natures.

Figure 3 shows how the spectra tend to vary with the probe position and sample size. For the large bundle of diameter ~14 nm, the BP shows up strongly when the probe is placed in the middle of the material, and the other excitations, while present, are difficult to separate from each other. When the probe was placed at the edge of the material, the energies of all the excitations have decreased, and the bulk BP mode has lost much of its intensity, making the SP modes much more visible. For the large aloof impact parameter (which should excite only surface modes), the bulk-plasmon peak has vanished entirely, the higher-energy peaks have decayed considerably, and the lower-energy peaks are still coming through strongly. This agrees qualitatively (and, as we shall see below, quantitatively) with the prediction that the intensity of a peak in the aloof case for a cylindrical geometry will vary with impact parameter b roughly as $\exp(-2b\omega/v)$, with v the speed of the passing electron and ω the angular frequency of the excitation.[35,36,38,47] The interband transition, which had previously been almost smothered by the tails of the zero-loss and π plasmon peaks, finally comes into its own as a clearly identifiable separate excitation at the large impact parameter. Thus by choosing where to place the electron beam, we choose which excitations will be most strongly represented in the spectrum.

At the other extreme, an isolated single-walled tube of diameter ~1.2 nm shows only a very weak BP, which is difficult to measure precisely. The SP scattering probabilities are very weak (especially at large impact parameters), and the PI moderately weak, while the IB peak is still quite strong. These spectra are shown with the background removed, and are left un-normalized to allow the viewer to estimate the effect of counting statistics. We should reiterate that the intensity in the 2–4-eV range does not appear when subtracting the background from a pure-background spectrum—the intensity we have identified with the IB peak does come from the sample. These plots should make it clear why the parameters for the IB peak cannot be known precisely from our measurements. For all of the peaks, the low signal-to-noise ratio makes it difficult to extract clear trends from the data. SP1 and SP2 are often difficult to distinguish at large impact parameters.

The trends that appear in Fig. 3 are representative of the behavior of our entire data set. We shall spend the rest of this section describing these trends in detail.

In the quasiclassical image-charge formalism with a cylindrical geometry, the $\exp(-2b\omega/v)$ functional form tends to hold rather well for the peak heights unless ω, b, and the cylinder radius R are all quite small.[36] The theoretical discrepancy is generally smaller than our experimental uncertainties. Figure 4 illustrates this with the experimental peak heights B_j for the bundle of diameter 14 nm, as a function of impact parameter relative to the edge of the material (with negative values intersecting the material). The BP unsurprisingly, is strongest in the middle of the bundle and drops to near invisibility as the center of the probe is moved just outside the edge of the material. The two SP modes are strong within the material, with SP2 stronger near the center and SP1 apparently strongest near the edge. Both drop off rapidly in the aloof region. The two low-energy peaks are fairly uniform within the material and drop off more slowly in the aloof region. We define $C_j = B_j \exp(2b\omega/v)$ and plot the C_j in Fig. 5, showing that much of the variation of intensity with position is accounted for by the predicted exponential law. We therefore take the C_j to be measures of the intrinsic excitability of each of the surface modes. For each sample diameter, we take the average C_j for each mode (weighted according to the uncertainties as discussed by Bevington[48]), and plot the results versus material diameter in Fig. 6. We also plot the bulk-plasmon B_j values as measured in the centers of the subjects. The parameters for the power-law trend lines are given in Table II. Much the same trends appear if we use the areas A_j rather than the peak heights B_j.

These plots show some very suggestive trends. All of the modes show roughly a power-law dependence of intensity on diameter, with two very noticeable outliers, one for SP1 at 14 nm and the other for SP2 at 11 nm. The two regression lines on these plots show power-law curve fits (with uncertainties

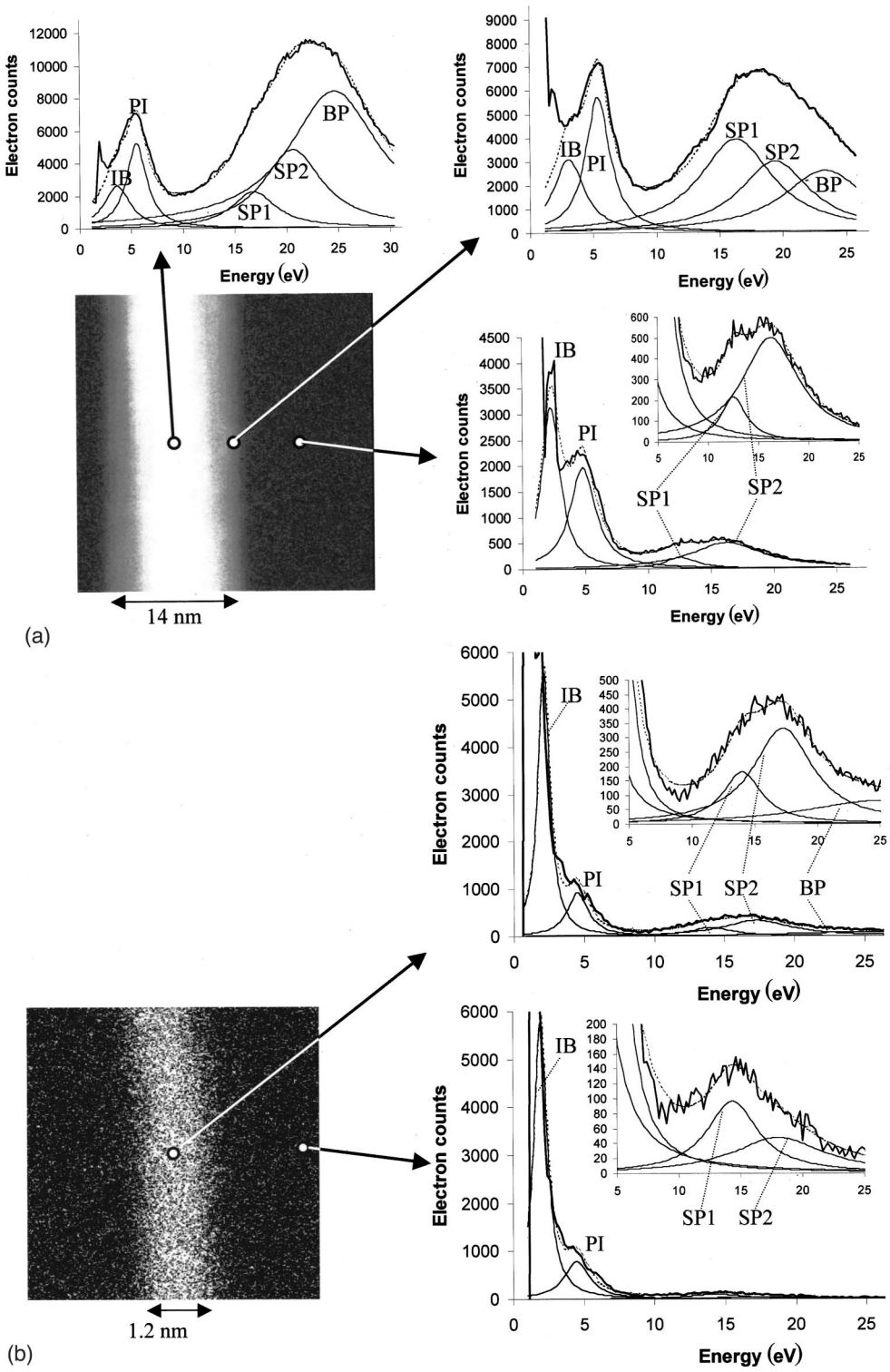

FIG. 3. STEM annular dark-field images showing measurement locations and the associated spectra, with background subtracted and Lorentzian decompositions. Dashed lines are the sum of all Lorentzian curves. Insets are close-ups of the same data. Identifiers are as in Table I. We include two subjects: (a) An inhomogeneous 14-nm-diameter bundle and (b) a single 1.2-nm-diameter tube.

in each data point accounted for) with and without the outliers. A potential explanation for the discrepancy presents itself for the 14-nm-diameter bundle, shown in STEM ADF in Fig. 3(a). This particular subject consists of a dense core and a much less dense outer sheath, which presumably has gaps among the tubes in the bundle. The appearance is uniform along the length of the bundle. It may be that this inhomogeneity affected the $\pi+\sigma$ surface plasmon in one of the two polarizations. The energies and widths of the $\pi+\sigma$ modes also show anomalies for this bundle, as shown below.

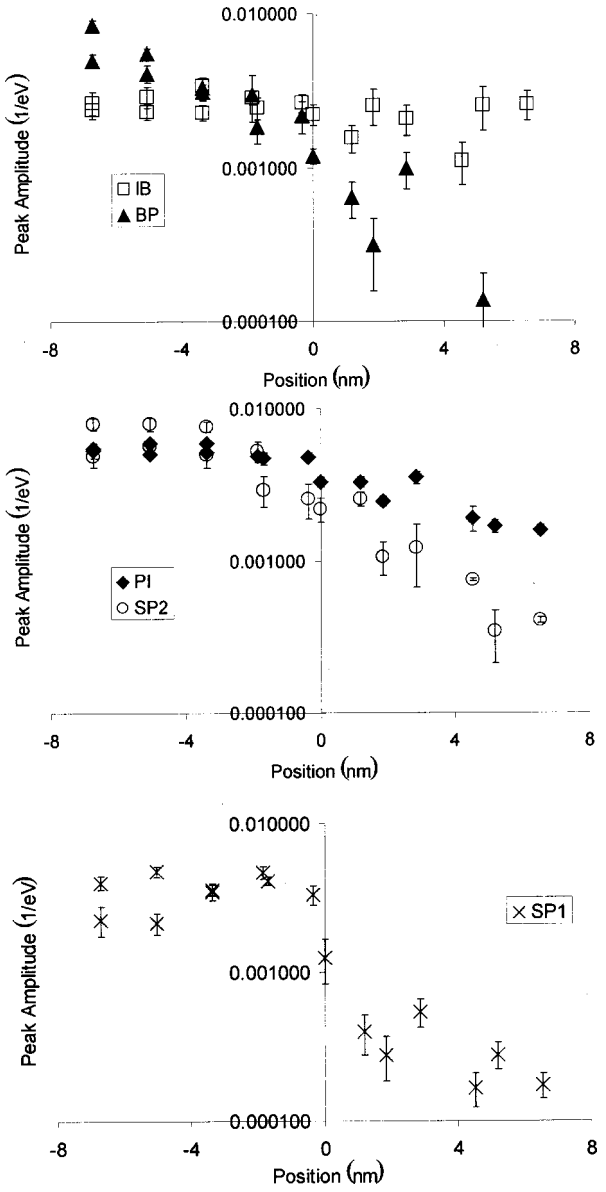

FIG. 4. Peak heights versus impact parameter relative to the edge of the material for the 14-nm-diameter bundle.

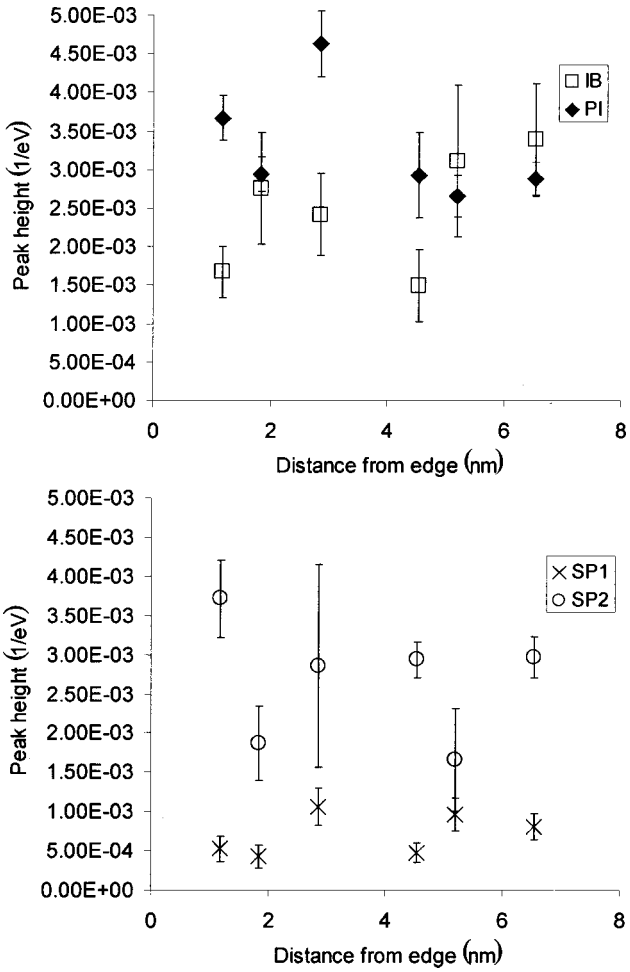

FIG. 5. Peak heights for aloof measurements of the 14-nm-diameter bundle, multiplied by $\exp(2b\omega/v)$. Comparison with Fig. 4 shows that this accounts for most of the positional variation.

Theoretical work is in progress to determine the plausibility of this explanation. The other outlying data point is one for which we have no explanation; we merely present curve fits with and without this point, letting the reader be the judge.

The exponents in the power laws are close to one for the ordinary surface plasmons, but closer to one-half for the interband transition, and 1.3 for the bulk plasmon. One simple theory predicts approximate exponents closer to 1.5–2.0 for all of the surface modes, assuming a classical dielectric function essentially like that of graphite.[36] Further theoretical work may be needed to explain this discrepancy. In any case, the power-law fits do not account for all of the variation in the data except perhaps in the SP2 case (with the unexplained outlier removed), as is clear from the χ^2/v values in Table II and the size of the error bars in Fig. 6 (which are smaller than the symbols in many cases).

There is a moderately strong tendency for the π-related peaks (the IB and PI) to show more scatter at smaller diameters, to a maximum in the limit of a single tube, while there is no such trend in the three $\pi+\sigma$ excitations. This may be caused by the sensitivity of the π bands to the chiral vector. We already know that the chiral angles in this particular sample vary randomly from one tube to another in this sample,[23] and we may simply be seeing an effect of particular chiral vectors that tends to average out as more tubes are included. It is reportedly possible to produce samples, which are primarily composed of nanotubes with a single chiral vector.[49] If the π excitations hold more strongly to the trend line for such a sample, this would lend credence to our proposed explanation, which so far is merely hinted at by the data but not firmly established.

The energies of the five excitations listed in Table I vary with the impact parameter and sample diameter. In Fig. 7, we compare the behavior in the extreme cases of a large bundle and a single isolated tube. The energy variation of the IB peak was not meaningfully measured, due to the influence of the PI peak on the curve fits. For the large inhomogeneous bundle (the one that produced the SP1 outlier in Fig. 5), the plasmons all show a higher energy in the penetrating than in the aloof case. The π plasmon increases from ~4.9 to 5.4 eV

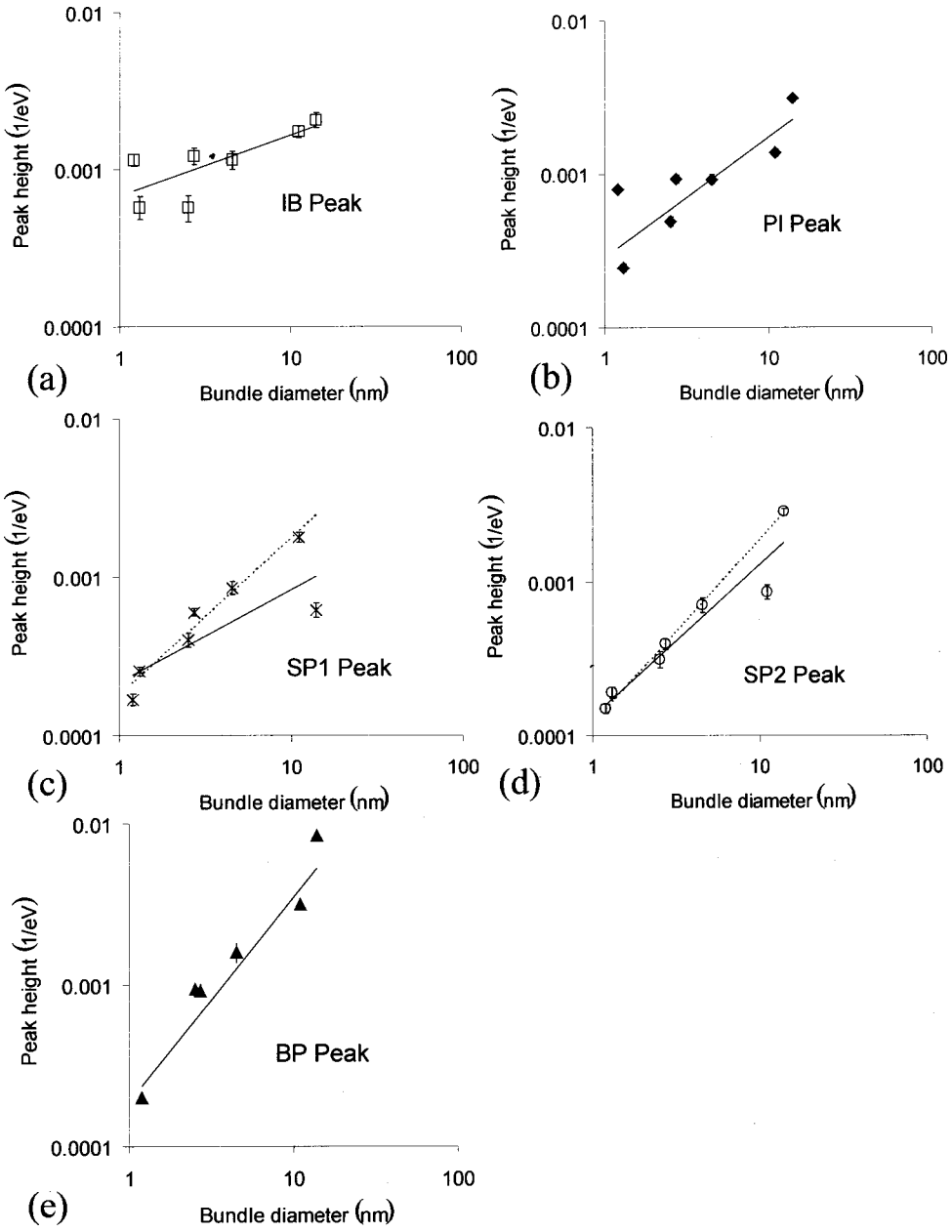

FIG. 6. Averaged exp($2b\omega/v$)-multiplied aloof-measured peak heights C_j as a function of material diameter for the five Lorentzians. The 1.2- and 1.3-nm materials are single tubes, the 14-nm material is a bundle of nonuniform density, and the remaining materials are homogeneous-looking bundles of roughly 3 to 100 tubes. Solid trend lines include all data points; dashed trend lines discount the most prominent outlying point. The BP peak height measured in the center of the bundle is also included. (a) IB, (b) PI, (c) SP1, (d) SP2, and (e) BP.

(possibly due to increased intermixing of the bulk mode), SP1 from 12.6 to 17 eV, SP2 from 16.2 to 21.5 eV, and the BP from 23 eV at the edge to ~26 eV in the center (which is similar to the anisotropy effect noted by Kociak *et al.*,[19] but probably has a different cause). This was the only bundle that showed large shifts in energy between the exterior and interior, as shown in Fig. 8. This was also the only bundle with an apparent density inhomogeneity in the STEM images. This suggests that the additional interface between the low- and high-density materials in this bundle has altered the nature of the surface plasmons, probably by introducing higher-energy modes that are combinations of the modes at the two interfaces.

The single tube shows quite a different result. The π plasmon occurs at ~4.2–4.5 eV for aloof measurements, climbing to ~5.2 eV as we penetrate the material. The two SP modes are difficult to separate from each other, especially at large impact parameters. The lack of total independence of the fit parameters for the two SP peaks is evident in the figure—this is a case in which the off-diagonal components of the error matrix are significant. The SP energies are 14–15 and 18–19 eV, with any positional variation hidden by the

TABLE II. Parameters for the trend lines in Fig. 6. Rows marked with an asterisk show the curve fits with the most prominent outlying point removed.

Peak	C_j at 1-nm diameter (10^{-4} eV^{-1})	Exponent	χ^2/ν
IB	6.8 ± 1.8	0.39 ± 0.13	7.6
PI	2.9 ± 1.3	0.78 ± 0.20	88.3
SP1	2.2 ± 0.9	0.58 ± 0.21	34.9
SP1*	1.8 ± 0.3	1.00 ± 0.11	7.1
SP2	1.3 ± 0.4	0.98 ± 0.15	19.2
SP2*	1.2 ± 0.1	1.18 ± 0.04	1.04
BP	1.9 ± 0.6	1.26 ± 0.14	19.3

limited reproducibility of the measurement. A few weakly measured BP data points at ~24 eV appear at impact parameters less than 0.8 nm. Since nonpenetrating electrons should not excite the bulk plasmon, this suggests that our 0.2-nm FWHM probe had a significant halo.

Figure 8 summarizes the energies and widths of the five peaks for the various tubes and bundles. We present the average values for aloof and penetrating electrons (labeled ''outside'' and ''inside'' on the graphs), not including data points at the edge where the energies and widths are in transition. Error bars are sample standard deviations of the means and are unrealistically small in a few cases due to relative scarcity of measurements. The parameters for the IB peak were not measured accurately but are included for completeness. For the externally measured PI peak energy, the single tubes (1.2- and 1.3-nm diameters) reach the extreme ends of the range, while the bundles all produce values of roughly 4.9 eV. The inside and outside PI energies are typically the same except for the largest bundles and the smaller single tube, where the interior PI energy increases significantly. The PI widths, all ~1.8–2.8 eV, do not show any strong trends.

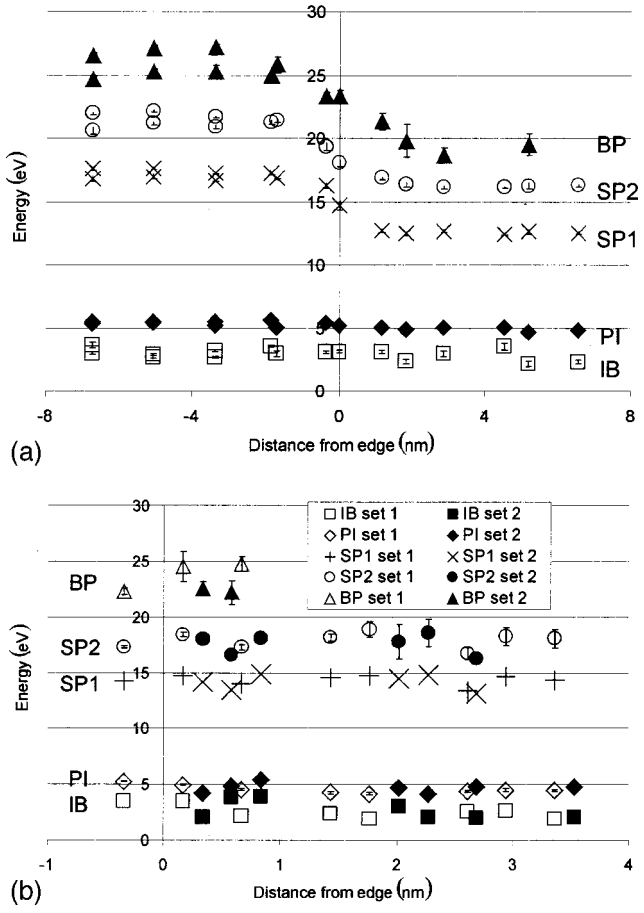

FIG. 7. Energies of the five peaks as a function of impact parameter for (a) the inhomogeneous 14-nm-diameter bundle, and (b) the 1.2-nm-diameter single tube. In (b), two data series from repeated experiments are represented with different symbols.

The SP1 peaks show roughly constant energies of 15 eV for all but the small single tube (which has a significantly lower energy) and the large inhomogeneous tube (in which the inside and outside modes have very different energies). The inside width tends to be lower, although this is reversed for the 14-nm bundle, yet another case where this sample behaved unusually. The SP2 peaks show much the same trends as the SP1, albeit with more variation from bundle to bundle. Finally, the $\pi+\sigma$ bulk plasmons (BP peaks, which were not accurately measured in the aloof mode) show energies of 24–26 eV, widths of 10–13 eV, and only very weak trends as a function of diameter. For all of the excitations with accurate energy measurements, the smaller isolated tube produced the lowest energies, while the 1.3-nm-diameter tube tended to produce higher-than-average energies. Again we find that the single tubes tend to behave more idiosyncratically than do the bundles, although again the trend is not very strong. More measurements may be needed to determine whether this is a real phenomenon or an accident of our particular data sets, and to determine exactly what structural parameters are responsible for the variation that exists.

VI. CONCLUSION

We have presented systematic EELS measurements of nanotube bundles of various diameters and free-standing single nanotubes, for both penetrating and aloof impact parameters, and analyzed the resulting spectra into five distinct excitations ranging from 2 to 30 eV, using a sum-of-Lorentzians model. The resulting data sets constitute a library of the energies, amplitudes, and widths of the various excitations. This library may be tested quantitatively against theoretical predictions, as we have done to a limited extent. Some of the patterns in the data are easily explained with current theory, while others await a detailed theoretical treatment that may require consideration of anisotropy, inhomogeneity, spatial dispersion, intertube interactions, or the effect of the chiral vector on the π band. Inhomogeneity in the bundle density appears to have dramatic effects on the $\pi+\sigma$ plasmons. There is some evidence that the single tubes show more individuality than do the bundles, particularly in the π-band-related excitations, which may be due to variations in the chiral vector.

It is essential in a study like this to systematically control the geometrical parameters—in this case the bundle diam-

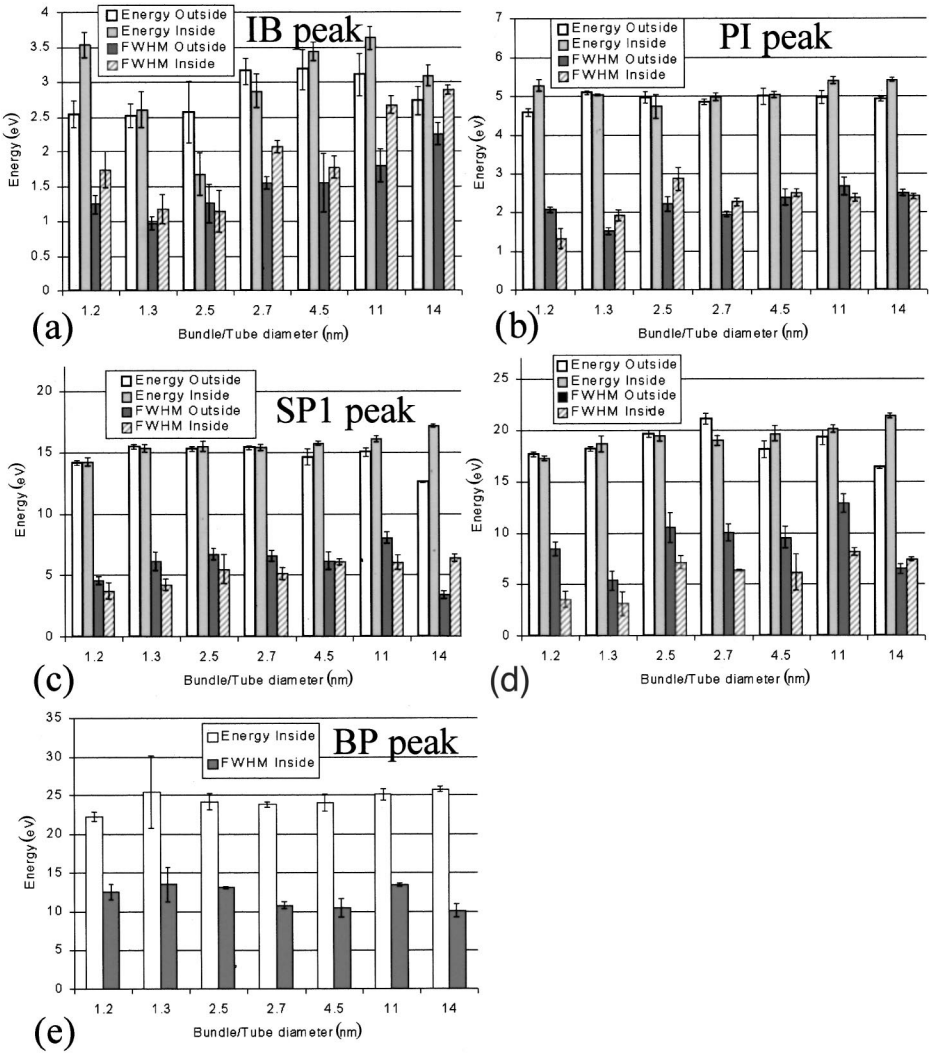

FIG. 8. Average energies and FWHM widths of the five excitations with the beam placed outside and inside the material. Error bars are sample standard deviations of the means. (a) IB, (b) PI, (c) SP1, (d) SP2, and (e) BP.

eter, the impact parameter, and the proximity of material other than the chosen nanotube. It is essential to keep other nanotubes at least several tens of nanometers from the measurement site, particularly for the low-energy excitations. The relative mix of surface and bulk signals depends greatly on the geometry, and this must be controlled in order to intelligently interpret the results. Different excitations appear most strongly under different geometrical conditions, and this will affect the design of an experiment that is particularly interested in only one or a few excitations. The problems of radiation damage, sample heating (and consequent moving), and contamination pinning are greatly reduced if one can acquire spectra without the beam penetrating the material.

It is also essential to be very careful with data analysis. Improper subtraction of background, estimates of uncertainties, and curve-fit models can produce meaningless trends, or restrict one's ability to judge the meaningfulness of the trends that appear. In the future, we should like to improve upon the techniques we have employed, incorporating the results of current efforts in spectral imaging analysis. We should emphasize that there are some features in the spectra that are not well modeled by the sum-of-Lorentzians function, and that these are particularly strong for penetrating spectra of large bundles. We may be able to quantify these features by using a more general data analysis technique. The sum-of-Lorentzians function works remarkably well in most cases, however.

The techniques we discuss are generally applicable to nanoscale systems. So far we have characterized a number of low-energy surface and bulk excitations in single-walled carbon nanotubes and bundles thereof. We already know from the literature that the results are significantly different for bent, multiwalled, and boron-nitride tubes, in ways that reflect the anisotropy and chemical bonding that appear in these systems. Nanotubes that are filled or coated with other material, which include *Y* junctions or accessible hemispherical caps, or that are predominantly of one chiral vector, should also provide interesting results. Nanowires of various materials will also be of interest, as will quantum dots. Quantum confinement may play a role in determining the widths, energies, and excitation amplitudes of the plasmons and interband transitions in these systems.[24] This interesting physics is within the reach of current STEM/EELS technology, and with upcoming improvements in both energy and spatial resolution, the phenomena may be studied in ever greater detail.

ACKNOWLEDGMENTS

We would like to thank Professor John Silcox and his associates at Cornell University, particularly Mick Thomas and Earl Kirkland, for the use of the UHV-STEM facility, operation of the microscope, and assistance in understanding of the behavior of the instrument. The nanotube material was provided by Professor Larry Dalton (Chemistry, University of Washington) and his collaborators. We would also like to thank Professor George Bertsch (Physics, University of Washington) for useful discussions concerning the theory. This work was supported by NSF Grant No. DMR 9978835.

[1] L. Chico, W. H. Crespi, L. X. Benedict, S. G. Louie, and M. L. Cohen, Phys. Rev. Lett. **76**, 971 (1996).
[2] S. Frank, P. Poncharal, Z. L. Wang, and W. A. de Heer, Science **280**, 1744 (1998).
[3] S. J. Tans, A. R. M. Verschueren, and C. Dekker, Nature (London) **393**, 49 (1998).
[4] R. Saito, M. Fujita, G. Dresselhaus, and M. S. Dresselhaus, Phys. Rev. B **46**, 1804 (1992).
[5] J. W. Mintmire and C. T. White, Carbon **33**, 893 (1995).
[6] M. F. Lin and D. S. Chuu, Phys. Rev. B **57**, 10 183 (1998).
[7] T. Stöckli, Z. L. Wang, J.-M. Bonard, P. Stadelmann, and A. Châtelain, Philos. Mag. B **79**, 1531 (1999).
[8] C. H. Olk and J. P. Heremans, J. Mater. Res. **9**, 259 (1994).
[9] J. W. G. Wildöer, L. C. Venema, A. G. Rinzler, R. E. Smalley, and C. Dekker, Nature (London) **391**, 59 (1998).
[10] T. W. Odom, J.-L. Huang, P. Kim, and C. M. Lieber, Nature (London) **391**, 62 (1998).
[11] R. Kuzuo, M. Terauchi, and M. Tanaka, Jpn. J. Appl. Phys., Part 2 **31**, L1484 (1992).
[12] R. Kuzuo, M. Terauchi, M. Tanaka, and Y. Saito, Jpn. J. Appl. Phys., Part 2 **33**, L1316 (1994).
[13] V. P. Dravid, X. Lin, Y. Wang, X. K. Wang, A. Yee, J. B. Ketterson, and R. P. H. Chang, Science **259**, 1601 (1993).
[14] P. M. Ajayan, S. Iijima, and T. Ichihashi, Phys. Rev. B **47**, 6859 (1993).
[15] S. L. Cullen, G. Botton, A. I. Kirkland, P. D. Brown, and C. J. Humphreys, Inst. Phys. Conf. Ser. **138**, 79 (1993).
[16] O. Stéphan, P. M. Ajayan, C. Colliex, F. Cyrot-Lackmann, and É. Sandré, Phys. Rev. B **53**, 13 824 (1996).
[17] T. Stöckli, J.-M. Bonard, P.-A. Stadelmann, and A. Châtelain, Z. Phys. D: At., Mol. Clusters **40**, 425 (1997).
[18] L. A. Bursill, P. A. Stadelmann, J. L. Peng, and S. Prawer, Phys. Rev. B **49**, 2882 (1994).
[19] M. Kociak, L. Henrard, O. Stéphan, K. Suenaga, and C. Colliex, Phys. Rev. B **61**, 13 936 (2000).
[20] T. Stöckli, J.-M. Bonard, A. Châtelain, Z. L. Wang, and P. Stadelmann, Phys. Rev. B **61**, 5751 (2000); Z. L. Wang (private communication).
[21] T. Hayashi, T. Kuzumaki, K. Miyazawa, and K. Ito, Mol. Cryst. Liq. Cryst. Sci. Technol., Sect. A **340**, 395 (2000).
[22] T. Pichler, M. Knupfer, M. S. Golden, J. Fink, A. Rinzler, and R. E. Smalley, Phys. Rev. Lett. **80**, 4729 (1998).
[23] B. W. Reed, M. Sarikaya, L. R. Dalton, and G. F. Bertsch, Appl. Phys. Lett. **78**, 3358 (2001).
[24] P. E. Batson and J. R. Heath, Phys. Rev. Lett. **71**, 911 (1993).
[25] S. Holst and W. Legler, Z. Phys. D: At., Mol. Clusters **25**, 261 (1993).
[26] H. Cohen, T. Maniv, R. Tenne, Y. Rosenfeld Hacohen, O. Stephan, and C. Colliex, Phys. Rev. Lett. **80**, 782 (1998).
[27] O. L. Krivanek, N. Dellby, and A. R. Lupini, Ultramicroscopy **78**, 1 (1999).
[28] P. E. Batson, Microsc. Microanal. **6**, 108 (2000).
[29] A. A. Lucas, L. Henrard, and Ph. Lambin, Phys. Rev. B **49**, 2888 (1994).
[30] A. Howie and R. H. Milne, Ultramicroscopy **18**, 427 (1985).
[31] Z. L. Wang, Micron **27**, 265 (1996).
[32] F. J. García de Abajo and J. Aizpurua, Phys. Rev. B **56**, 15 873 (1997).
[33] P. Moreau, N. Brun, C. A. Walsh, C. Colliex, and A. Howie, Phys. Rev. B **56**, 6774 (1997).
[34] F. J. García de Abajo and A. Howie, Phys. Rev. Lett. **80**, 5180 (1998).
[35] G. F. Bertsch, H. Esbensen, and B. W. Reed, Phys. Rev. B **58**, 14 031 (1998).
[36] B. W. Reed, J. M. Chen, N. C. MacDonald, J. Silcox, and G. F. Bertsch, Phys. Rev. B **60**, 5641 (1999).
[37] A. Rivacoba, N. Zabala, and J. Aizpurua, Prog. Surf. Sci. **65**, 1 (2000).
[38] D. A. Muller and J. Silcox, Ultramicroscopy **59**, 195 (1995).
[39] M. F. Lin, D. S. Chuu, C. S. Huang, Y. K. Lin, and K. W.-K. Shung, Phys. Rev. B **53**, 15 493 (1996).
[40] A. Rubio, D. Sánchez-Portal, E. Artacho, P. Ordejón, and J. M. Soler, Phys. Rev. Lett. **82**, 3520 (1999).
[41] C. Yannouleas, E. N. Bogachek, and U. Landman, Phys. Rev. B **50**, 7977 (1994).
[42] A. G. Rinzler *et al.*, Appl. Phys. A: Mater. Sci. Process. **67**, 29 (1998).
[43] J. Liu *et al.*, Science **280**, 1253 (1998).
[44] P. E. Batson, Phys. Rev. Lett. **49**, 936 (1982).
[45] D. Ugarte, C. Colliex, and P. Trebbia, Phys. Rev. B **45**, 4332 (1992).
[46] V. E. Cosslett, in *Electron Microscopy and Analysis*, edited by T. Mulvey (Institute of Physics, Briston, 1980), p. 277.
[47] R. F. Egerton, *Electron Energy Loss Spectroscopy in the Electron Microscope*, 2nd Ed. (Plenum, New York, 1996).
[48] P. R. Bevington, *Data Reduction and Error Analysis for the Physical Sciences* (McGraw-Hill, New York, 1969).
[49] P. Nikolaev, A. Thess, A. G. Rinzler, D. T. Colbert, and R. E. Smalley, Chem. Phys. Lett. **266**, 422 (1997).